INSTITUTE OF PHYSICS PUBLISHING JOURNAL OF PHYSICS D: APPLIED PHYSICS

J. Phys. D: Appl. Phys. **38** (2005) 1633–1643 doi:10.1088/0022-3727/38/11/001

Modelling of microdischarge devices: plasma and gas dynamics

Mark J Kushner

Department of Electrical and Computer Engineering, Iowa State University, 104 Marston, Ames, IA 50011, USA

E-mail: mjk@iastate.edu

Received 1 December 2004, in final form 9 January 2005
Published 20 May 2005
Online at stacks.iop.org/JPhysD/38/1633

Abstract

Microdischarge devices (MDs) share many properties with their macroscopic counterparts while having unique features resulting from their ability to sustain large current densities and power depositions on a continuous basis at pressures approaching atmospheric. The dynamics of cylindrical, metal–dielectric–metal sandwich MDs sustained in Ar having characteristic sizes of a few hundred micrometres have been computationally investigated using a plasma-transport model which includes gas dynamics. We found that these devices closely resemble negative glow discharges, as they are sustained by, and particularly sensitive to, ionization resulting from secondary electron emission from the cathode. Since these MDs operate on a cw basis with large current densities and power deposition, gas heating and flow dynamics are important considerations in optimizing their electrical and kinetic properties. For example, the formation of excimer species is particularly sensitive to gas heating and rarefaction due to their dependence on three-body formation processes. Scalings of MDs with pressure, current and secondary emission coefficient are discussed.

1. Introduction

Microdischarge devices (MDs) are plasma sources that the leverage *pd* (pressure × characteristic dimension) of conventional glow discharges to operate on a continuous basis with dimensions of tens to hundreds of micrometres at gas pressures approaching and exceeding 1 atm. As such, the physics of MDs should, in principle, parallel their macroscopic counterparts [1–4]. Their small dimensions and resulting high gas pressures, though, enable MDs to access operational spaces that conventional macroscopic devices cannot. For example, cw operation of MDs at power depositions of tens of kW cm^{-3} is not uncommon, conditions which can only be accessed on a pulsed basis in macroscopic discharges. The resulting high current densities can produce significant gas heating and large momentum transfer from the electric field to the gas, thereby initiating gas dynamics. Unlike their larger counterparts, the size of MDs can approach the Debye length, λ_D, which potentially impacts the ability of the plasma to efficiently utilize the electrode structures. MDs are finding applications as visible and UV emitters and as chemical reactors [1–8].

In this paper, results from a computational investigation of the fundamental processes underlying operation of MDs and their unique attributes will be discussed. The particular MD structure of interest is a cylindrically symmetric design with a central hole through a sandwich consisting of a metal–dielectric–metal stack. (Although these MDs share many characteristics with the microdischarges used in plasma display panels cells, the latter are dielectric barrier discharges, and so are intrinsically pulsed devices [9]. Our interest here is in cw devices.) We found that typical MD devices having these characteristics do not operate as classical hollow cathodes. Their operation does, however, critically depend on the contributions of ionization from beam electrons accelerated in the cathode fall resulting from secondary electron emission following ion impact. As such, the devices resemble negative glows. Gas heating and the resulting gas rarefaction can significantly impact the rate of formation of excimer species which require three-body stabilization. The large steady state current densities (many A cm^{-2}) transfer significant momentum to the neutral gas, producing convective flow having speeds in excess of tens of metres per second. The

 © 2005 IOP Publishing Ltd Printed in the UK

model used in this study is described in section 2. Properties of sandwich MD devices are discussed in section 3. Concluding remarks are in section 4.

2. Description of the model

The model employed in this study is based on LAMPSIM, which is described in detail in [10–12]. LAMPSIM, is a multifluid, two-dimensional hydrodynamics model in which transport equations for all charged and neutral species and Poisson's equation are integrated as a function of time. The numerical grid uses a boundary fitting, unstructured mesh in order to resolve the fine spatial structure of MDs, as well as their larger surrounding structures. Updates of the charged particle densities and electric potential are followed, in a time splicing manner, with an implicit update of the electron temperature (by solving the electron energy equation), neutral particle densities, beam electron transport and flow field properties. The electron transport coefficients and rate coefficients for bulk electrons as a function of electron temperature are obtained by solving Boltzmann's equation for the electron energy distribution. These quantities are periodically updated during execution of the model as mole fractions change, which in turn affect the form of the electron distribution functions.

The transport of beam electrons emitted from the cathode are tracked using an electron Monte Carlo simulation (eMCS), as described in [11, 12]. The advancement of trajectories in the eMCS is performed on a Cartesian mesh (CM) that is overlaid onto the unstructured hydrodynamics mesh (UM). The CM overlays only that portion of the UM in which beam electron transport is expected to be important, a choice refined by iteration and experience. Electron pseudoparticles are periodically launched from specified surfaces having weightings proportional to the rate of secondary electron emission by ion or photon bombardment. By sampling the trajectories of the pseudoparticles, the electron energy distributions (EEDs) due to beam electrons are generated as a function of position. These EEDs are used to produce source functions for electron impact processes by beam electrons which are held constant until the next execution of the eMCS. Beam electrons and their progeny which slow below a specified energy threshold (usually 4 eV) are grouped into a source function for bulk electrons. The frequency at which the eMCS is executed is refined by iteration and experience, and is as short as every ns during the startup process to as long as 10–30 ns when steady state conditions are approached.

An improvement to the model described in [11] is including the production of secondary electrons from surfaces resulting from photoemission [12]. In this regard, the source of photoelectrons from surface points at location $\vec{r}_i$ on material m, $S_m(\vec{r}_i)$, due to photons emitted from location $\vec{r}_j'$ is

$$S_m(\vec{r}_i) = \sum_k \gamma_{mk} A_k \int N_k(\vec{r}_j') G_k(\vec{r}_j', \vec{r}_i) \mathrm{d}^3(\vec{r}_j'), \qquad (1)$$

$$G_k(\vec{r}_j', \vec{r}_i') = \frac{\exp(-\int_{\vec{r}_j'}^{\vec{r}_i'} \sum_l \sigma_{lk} N_l(\vec{r}_n') \mathrm{d}\vec{r}_n')}{4\pi \left|\vec{r}_j' - \vec{r}_i'\right|^2}, \qquad (2)$$

where N_k is the density of the kth radiating species having Einstein coefficient A_k, γ_{mk} is the photoemission probability for photons generated by species k incident on material m, and σ_{lk} is the total absorption cross section for photon k by species l. $G_k(\vec{r}_j', \vec{r}_i')$ is a Green's function for the survival of photons emitted at location $\vec{r}_j'$, $\vec{r}_i'$, and also accounts for view angles and obscurations.

Another improvement to the model described in [11] is that the fluid averaged advective velocity is obtained by solving a modified form of the compressible Navier Stokes equations in which source terms for momentum imparted from the electric field are included. In doing so, we assume that the pressure is sufficiently high and the rate of momentum transfer is sufficiently large that little momentum is instantaneously stored in the electrons and ions. As such, the electron and ion momentum sources instantaneously appear in the fluid equations. The equations we solve for the fluid averaged advective velocity, $\vec{v}$, are

$$\frac{\partial \rho}{\partial t} = -\nabla \cdot \rho \vec{v}, \qquad (3)$$

$$\frac{\partial \rho \vec{v}}{\partial t} = -\nabla P - \nabla \cdot \rho \vec{v} \vec{v}_i - \nabla \cdot \overline{\overline{\tau}} + \sum_i q_i N_i \vec{E}, \qquad (4)$$

$$\frac{\partial \rho c_p T}{\partial t} = -\nabla \cdot (-\kappa \nabla T + \vec{v} c_p T) - P(\nabla \cdot \vec{v}) + (\overline{\overline{\tau}} \cdot \nabla \vec{v}) - \sum_i \Delta h_i S_i + \sum_i \vec{j}_i \cdot \vec{E}, \qquad (5)$$

$$\frac{\partial \rho c_p T_m}{\partial t} = -\nabla \cdot (-\kappa_m \nabla T_m), \qquad (6)$$

where ρ is the total mass density (including charged species), T is the gas temperature, P is the thermodynamic pressure (ideal gas behaviour), $\overline{\overline{\tau}}$ is the viscosity tensor, κ is the thermal conductivity, c_p is the heat capacity, and Δh_i is the heat of formation for reaction i having source function S_i. Equations (3)–(5) are solved throughout the plasma volume. Equation (6), with the subscript m denoting non-plasma materials, is solved only in solids and non-plasma gases. The last term in equation (4) accounts for momentum imparted from the electrostatic field $\vec{E}$ where the sum is over all charged species having density N_i, and charge q_i. The last term in equation (5) accounts for joule heating due to acceleration of ions in the electrostatic field having current density j_i. The terms we retained in the viscosity expressions for momentum and energy are

$$\tau_{rr} = -\mu \left(2\frac{\partial v_r}{\partial r} - \frac{2}{3}\nabla \cdot \vec{v}\right),$$
$$\tau_{zz} = -\mu \left(2\frac{\partial v_z}{\partial z} - \frac{2}{3}\nabla \cdot \vec{v}\right), \qquad (7a)$$
$$\tau_{rz} = \tau_{zr} = -\mu \left(\frac{\partial v_z}{\partial r} + \frac{\partial v_r}{\partial z}\right),$$

$$(\overline{\overline{\tau}} \cdot \nabla \vec{v}) = \mu \left(\left(\frac{\partial v_r}{\partial r}\right)^2 + \left(\frac{\partial v_z}{\partial z}\right)^2\right). \qquad (7b)$$

Given the bulk fluid velocity, the densities of individual neutral species are obtained from

$$\frac{\partial N_i}{\partial t} = -\nabla \cdot \left(\vec{v} - D_i N_T \nabla \left(\frac{N_i}{N_T}\right)\right) + S_{Vi} + S_{Si}, \qquad (8)$$

where D_i is the mole fraction weighted diffusion coefficient, N_T is the total gas density, S_{Vi} is the source function due to

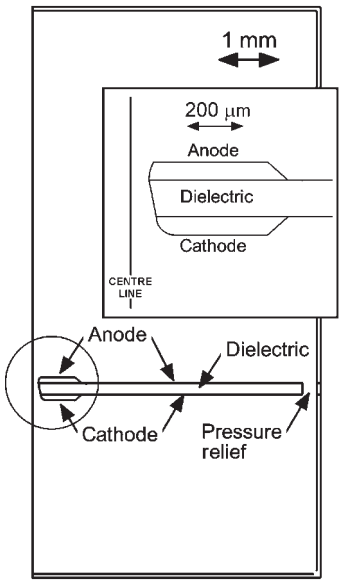

Figure 1. Schematic of the device for the base case. The geometry is cylindrically symmetric.

volumetric processes and S_{Si} is the source function due to surface processes. The surface source function is

$$S_{Si} = \sum_k -\eta_{ki}\,(\nabla \cdot \phi_k), \tag{9}$$

where ϕ_k is the flux of species k (charged and neutral) incident onto the surface and η_{ki} is probability of producing species i from incident species k.

The base case geometry used in this study, schematically shown in figure 1, is a cylindrically symmetric metal–dielectric–metal sandwich similar to the devices described in [1, 3]. The top electrode is the anode and the bottom electrode is the cathode. All external boundaries are metal with the exception of an insulating dielectric break between biased and grounded surfaces. The metal lining the lower plenum is held at the cathode potential while the metal lining the upper plenum is held at the anode potential. The central hole is 100 μm in radius at the anode, flaring to 150 μm near the cathode. The dielectric is 200 μm thick and the electrodes are 100 μm thick near the hole. (The decrease in thickness of the cathodes away from the hole is for computational convenience to reduce the number of mesh points. Tests were performed to confirm that this reduction in thickness does not affect the results.) The mesh contains 5424 nodes of which 3693 are in the plasma. The mesh resolution is 3–5 μm in the plasma channel, expanding to 100–150 μm near the boundaries.

There is no net flow of gas within the computational domain (i.e. no pumps or outlets). Since, as we will see, the MDs are themselves gas pumps a pressure relief channel was provided through the dielectric at the outer radius. This ultimately results in there being global gas circulation, as discussed below. The specified current is obtained by adjusting a ballast resistor while keeping the supply voltage constant. The gas is argon and the species included in the model are: e, Ar(3s) (argon ground state), Ar(4s), Ar(4p), Ar^+, Ar_2^* and Ar_2^+. The reaction mechanism is the same as that discussed in [12]. Secondary electron emission by ion impact was included only on the cathode with probability of $\gamma = 0.15$.

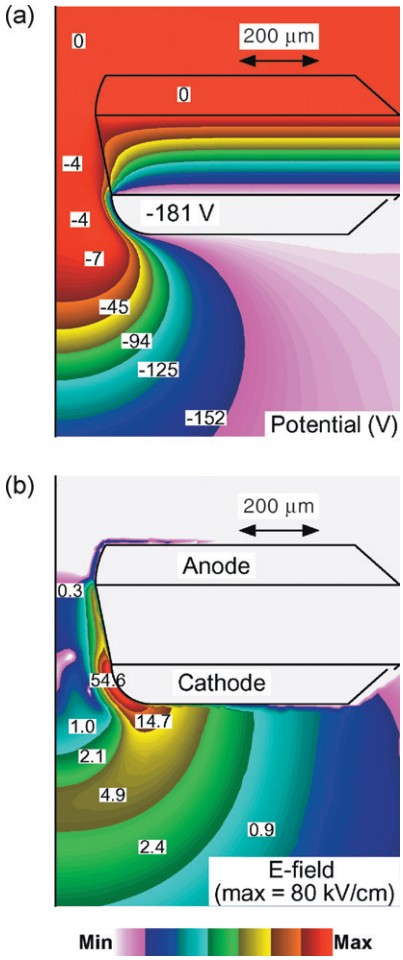

Figure 2. Electrical properties for a microdischarge sustained in 250 Torr Ar with a current of 2 mA. (*a*) Electric potential and (*b*) electric field (contour labels in kV cm^{-1}). The anode potential penetrates through the central hole, producing electric fields approaching 80 kV cm^{-1} at the cathode.

The MDs are operated in a cw mode, a condition obtained in the model by a time integration to the steady state. Different time steps or time intervals of integration are used in different modules in order to speed convergence. For example, in the fluid module the modified Navier–Stokes equations are integrated for periods of 0.05 to 1 μs for every 0.5 ns of integration of the plasma transport equations. Updates of these durations are then applied to individual neutral species. A typical case requires 1 day of CPU time on a high speed workstation (Hewlett Packard ES-47).

3. Characteristics of the cylindrical sandwich MDs

3.1. Characteristics of the base case

Electrical characteristics (potential and electric field) are shown in figure 2 for the base case operating conditions of 250 Torr Ar and 2 mA current. Plasma properties (electron temperature, electron sources and electron density) are shown in figure 3. The densities of ground and excited states of argon [Ar, Ar(4s) Ar(4p) and Ar_2^*] are shown in figure 4.

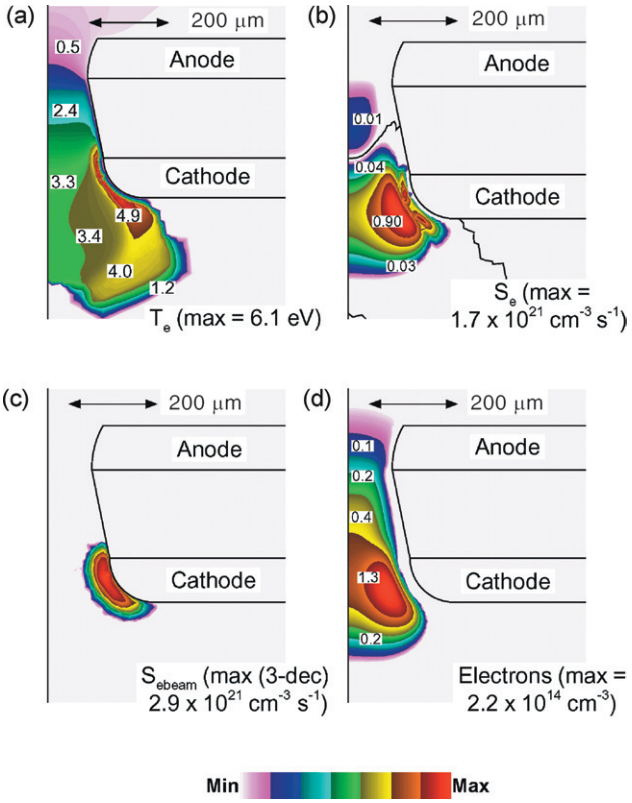

Figure 3. Plasma parameters for a microdischarge sustained in 250 Torr Ar (2 mA). (*a*) Electron temperature, (*b*) electron ionization source due to bulk electrons, (*c*) electron ionization source due to beam electrons and (*d*) electron density. With the exception of T_e, plots are two-decade log-scales. The maximum value for each frame is noted. The lines in the plot for the bulk sources separate regions of net positive sources and net negative sources, the latter due to dissociative recombination of Ar_2^+. Ionization by bulk and beam electrons have commensurate peak values.

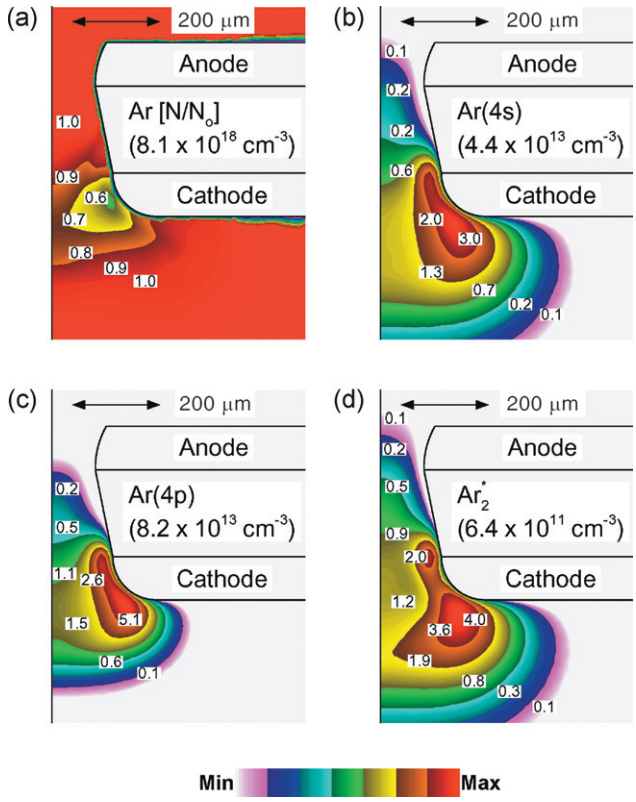

Figure 4. Species densities for a microdischarge sustained in 250 Torr Ar (2 mA). (*a*) Ar ground state density normalized by its ambient value, (*b*) Ar(4s), (*c*) Ar(4p) and (*d*) Ar_2^*. With the exception of Ar, plots are two-decade log-scales with maximum values noted. Gas heating produces a factor of two rarefaction in ground state density. As a result, the rate of formation of Ar_2^* is depressed near the cathode.

The anode potential deeply penetrates through the central hole, creating an electric field structure resembling a hollow cathode. The geometric electric field enhancement at the surface of the curved cathode is intensified by the compression of electric field lines by penetration of the anode potential through the cathode aperture. Peak electric fields near the cathode are in excess of 80 kV cm^{-1} or an E/N (electric field/gas number density) of 1600 Td (1 Td $= 10^{-17}$ V cm^2). Normalized electric fields near the centre of the channel are 5–20 Td. The resulting bulk electron temperature, T_e, is 5.5–6.0 eV near the cathode, falling to 2–3 eV near the centre of the channel. These moderate electron temperatures, aided by the multistep ionization enabled by the large Ar(4s) density ($>10^{13}$ cm^{-3}), produce source functions for ionization by bulk electrons peaking at 1.7×10^{21} cm^{-3} s^{-1}. The predicted metastable densities are commensurate with those measured experimentally [3].

Ion bombardment of the cathode releases secondary electrons that are accelerated in the large electric fields in the cathode fall. Based on the diameter of the hole at the cathode, $pd = 7.5$ Torr cm, which is too large for the beam electrons to penetrate completely across the gap with this voltage. As a result, the device does not operate as a classical hollow cathode. Ionization by secondary electrons is therefore limited to the vicinity of the cathode with a peak value of 2.8×10^{21} cm^{-3} s^{-1}. The combined sources from bulk and beam electrons produce a peak electron density of 2.1×10^{14} cm^{-3} in an annulus around the cathode. The annulus is enabled by there being significant volumetric losses to dissociative ionization with Ar_2^+. To sustain 2 mA, the cathode–anode potential is -181 V, which compares favourably to similar experimental devices [1, 3].

Even though the MD is not a classical hollow cathode, ionization by beam electrons is nevertheless critical to operation of the MD. As such, their characteristics resemble those of negative glows. Parametrizations were performed in which photoemission of electrons from the cathode resulting from photon transport from excited states was included and excluded. The photoemission probability and absorption cross sections were varied over a range of physically realizable values. For these conditions, we did not find that the resulting ionization by electrons originating from photoemission was critical to the operation of the MDs. This should not, however, be considered a general result. The electronic band-bending that occurs at the surface of the cathode resulting from the large electric fields in the adjacent plasmas could significantly alter the photoemission properties. These effects were not taken into consideration.

The distributions of visible photon emitters (as represented by the Ar(4p) density) and UV photon (excimer) emitters (as represented by the Ar_2^* density) are shown in figure 4. Similar

to the plasma density, the density of emitters is largely annular. The visible emitters (Ar(4p)) have a more restricted radial distribution compared to the excimer emitters (Ar_2^*). The lifetimes of the visible emitting states are at best a few hundred nanoseconds, and their excitation occurs dominantly in the high electric field region near the cathode either by the bulk or beam electrons. Due to their short lifetimes, the Ar(4p) states do not transport far from where they are formed before radiating and so have an annular distribution. Although the Ar_2^* state has a lifetime of only 17 ns, it is formed by three-body collisions of the more widely distributed metastable Ar(4s). As the rate of quenching of the metastable is slow and advection aids in its distribution, Ar(4s) is able to convect many tens to a few hundred micrometres from the high electric field region near the cathode before being lost. The formation of Ar_2^* and its radiation is therefore more widely distributed.

The operation of MDs encompass not only plasma transport but also gas dynamics. Momentum imparted to the ions by the electric field is transferred to neutrals through inelastic (charge exchange) and elastic collisions in less than 1 ns at 250 Torr. The end result is a system in which gas heating can be significant and momentum transfer may produce considerable gas pumping. For example, the gas temperature, gas speed and gas flow field are shown in figure 5 for the base case. (The Ar ground state density is shown in figure 4*a*.) The steady state current density near the cathode is 5–10 A cm^{-2} producing power deposition of tens of kW cm^{-3}. The resulting joule heating produces a peak gas temperature of 580 K. (In these examples, the temperatures of the bounding materials were held constant at 300 K. As these materials would likely heat during actual MD operation, the more pertinent thermodynamic value is the gas heating above ambient, which for this example is 280 K.) The end result is rarefaction of nearly a factor of 2 near the cathode. This rarefaction aids in extending the range of secondary electrons emitted from the cathode.

The rate of gas heating critically depends on the fraction of the ion momentum in the cathode fall that is dissipated by collisions and what proportion is ballistically dissipated by colliding with the cathode. For these results, the local heating rate by ions was simply $\vec{j} \cdot \vec{E}$, and so assumes that collisional dissipation dominates. A more accurate allocation of ion momentum between collisions and a ballistic component would require a kinetic formulation for ion transport.

For the conditions of interest, the net body force, $\vec{F}_b$ from charged particles to the neutral gas is approximately [13]

$$\vec{F}_b = \sum_i (q_i N_i \vec{E} - \nabla p_i - m_i v_{di} S_i), \qquad (10)$$

where the sum is over charged particles p_i is the charged particle thermodynamic pressure, v_{di} is the drift velocity and S_i is the particle source function. Assuming that all momentum acquired by charged particles is ultimately transferred to the gas (or surfaces) through collisional processes, all terms have maximum values in the vicinity of the cathode where electric fields, charged particle gradients and source functions are largest. For our conditions, the source of momentum by net acceleration in the electric field is largest by approximately a factor of 10 over that due to the pressure gradient, which is in turn larger by approximately a factor of 10 over that due to ionization.

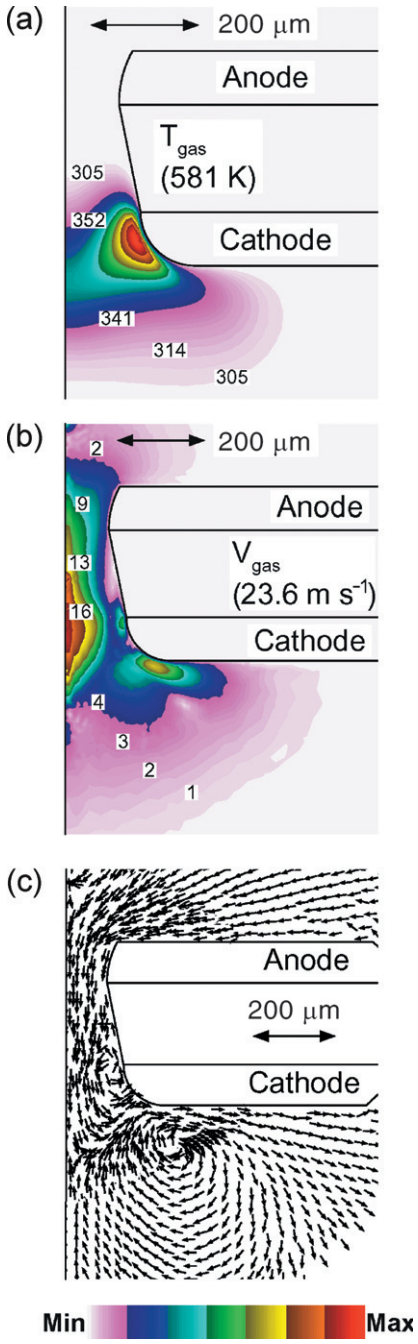

Figure 5. Fluid properties for a microdischarge sustained in 250 Torr Ar (2 mA). (*a*) Gas temperature, (*b*) magnitude of the fluid velocity and (*c*) vector direction of fluid velocity. (Arrows show direction only; not magnitude.) Joule heating raises the gas temperature 280 K above ambient. With there being no impressed gas sources or pumping, ion momentum transfer accelerates gas through the hole, producing on axis speeds in excess of 23 m s^{-1}.

The net transfer of momentum to the gas from the electric field scales with the net charge density. In the bulk plasma where the charge density is small, the net momentum transfer is also small. For this device, the momentum imparted to ions is generally directed vertically downward towards the edge of the cathode where the cathode directed electric fields

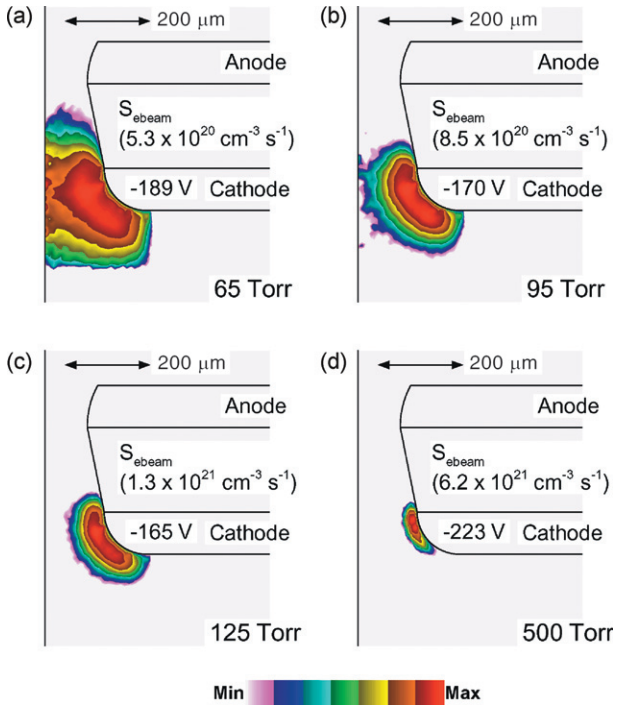

Figure 6. Electron ionization sources by secondary beam electrons for microdischarges sustained in Ar (2 mA) for (*a*) 65 Torr, (*b*) 95 Torr, (*c*) 125 Torr and (*d*) 500 Torr. (See figure 3 for 250 Torr.) All are two-decade log-scale plots with maximum values indicated, as is the cathode voltage. For pressures <200 Torr, the cathode voltage increases while the stopping power of beam electrons decreases producing broader regions of beam ionization.

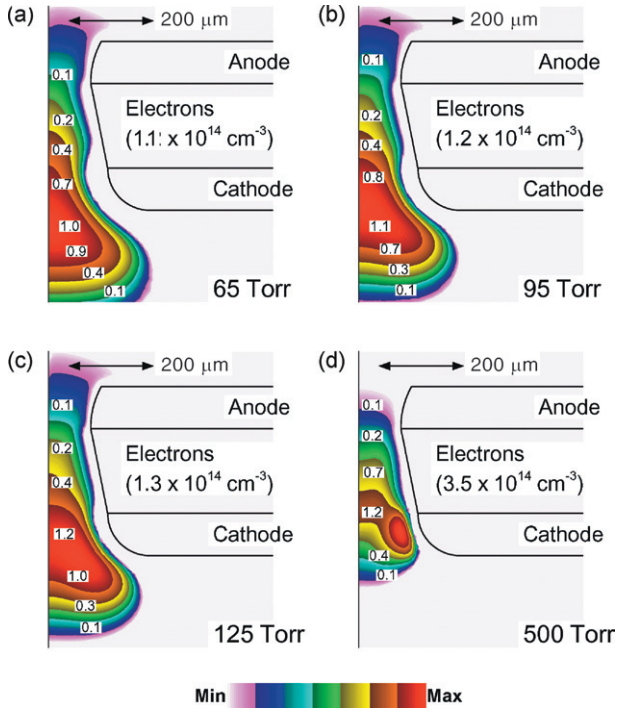

Figure 7. Electron density for microdischarges sustained in Ar (2 mA) for (*a*) 65 Torr, (*b*) 95 Torr, (*c*) 125 Torr and (*d*) 500 Torr. (See figure 3 for 250 Torr.) All images are two-decade log-scale plots with maximum values indicated. The electron density peaks on axis at pressures <125 Torr. The progressively off-axis peak in density at higher pressure is due to the more confined beam ionization and there being a larger proportion of Ar_2^+ producing volumetric recombination.

are largest. As the charge density becomes positive near the cathode, net momentum is transferred to the neutral gas, which is entrained and accelerated downwards through the aperture, as shown in figure 5. As such, the microdischarge acts very much like a pump; gas is extracted from the plenum above the MD and expelled into the plenum below the MD. Peak axial speeds of the neutral gas exceed 23 m s^{-1}. In this particular configuration, the momentum transfer provides a shearing force. When combined with the gas in the lower plenum being essentially stagnant, recirculation zones are generated. The end result is a lateral and downward expulsion of gas. Pressure stabilization is ultimately enabled by the relief hole. This results in a global circulation of gas down and through the MD channel into the lower plenum; and upwards through the relief slot into the upper plenum.

3.2. Plasma properties for different pressures

Ionization sources due to secondary beam electrons and the electron density are shown in figures 6 and 7 for pressures of 65–500 Torr while keeping the current constant at 2 mA. (See figure 3 for results at 250 Torr.) The cathode voltage and peak electron density as a function of pressure are shown in figure 8. Over the pressure range investigated, the cathode voltage required to sustain 2 mA has a minimum magnitude of −165 V at approximately 125 Torr, mimicking Paschen law behaviour. In spite of the increasing cathode voltage above 125 Torr, the range of electrons accelerated in the cathode fall is small, and so sources of ionization by beam electrons are confined to be near the cathode. For example, ionization sources are significant only within 20 μm of the cathode at 500 Torr.

More extended ionization sources by secondary electrons are obtained at pressures below 125 Torr due to the increasing cathode voltage and lower stopping power of the gas. There is also more rarefaction of the gas at lower pressures that aids in extending the range of the beam electrons. The gas temperature is up to 200 K higher in the middle of the channel at 50 Torr compared to 500 Torr. At no time, however, is there a classic hollow cathode effect where the range of the beam electrons is commensurate to or exceeds the diameter of the cathode. In this regard, the devices operate more like negative glows than hollow cathodes.

The end result is that the electron density peaks in an annulus at pressures exceeding 200 Torr. At lower pressures, the peak in electron density is on axis. The peak electron density monotonically increases from 50 Torr (1×10^{14} cm^{-3}) to 625 Torr (3.7×10^{14} cm^{-3}), due in large part to the more tightly confined sources of ionization by secondary electrons. Note that the cathode fall (denoted by the absence of electrons near the cathode in figures 3 and 7) thins as the pressure increases. The cathode fall is thickest at the lowest pressures due to the large cathode voltage and lower electron density. The cathode fall thins at higher pressures due in part to the larger electron density and in part to the reduced range of secondary electrons.

The peak densities of Ar(4p) and Ar_2^* are shown in figure 8 as a function of pressure. The spatial distributions of these states are shown in figure 9 for pressures of 50, 125 and 500 Torr. (See figure 4 for 250 Torr.) The peak Ar(4p)

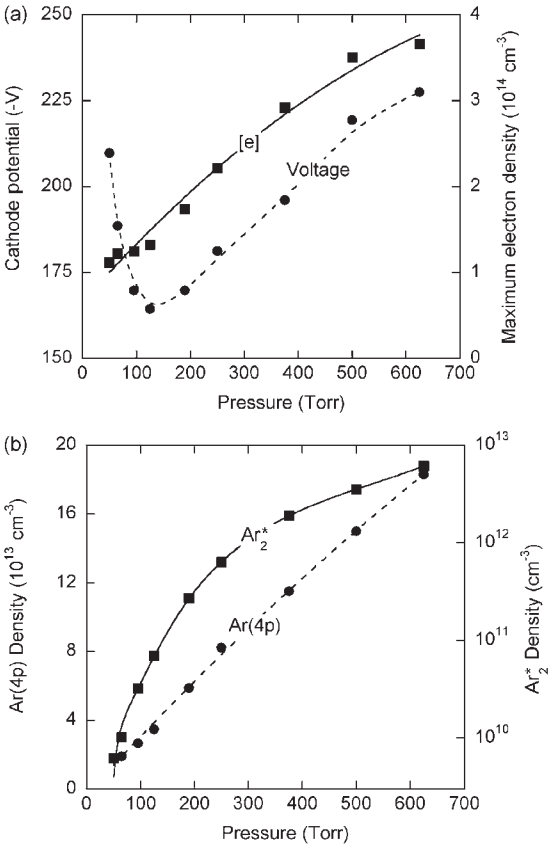

Figure 8. Plasma parameters as a function of pressure for microdischarges sustained in Ar (2 mA). (*a*) Cathode voltage and peak electron density. (*b*) Maximum densities of Ar_2^* and Ar(4p). Peak values of electron and excited state densities increase with pressure due to there being more confined electron impact source by beam electrons. Ar_2^* increases logarithmically due to its three-body formation mechanism.

density increases approximately linearly with pressure from 2×10^{13} cm^{-3} at 50 Torr to 1.8×10^{14} cm^{-3} at 625 Torr. This increase in peak density is a consequence of the increase in peak power deposition by beam electrons with pressure as the range of secondary electrons decreases. The peak density of Ar_2^* is 6×10^{12} cm^{-3} at 625 Torr, falling to 6×10^{9} cm^{-3} at 50 Torr. This large dynamic range principally results from Ar_2^* being formed by a 3-body collision process, whose rate scales with the square of the Ar density, and so rapidly falls as the pressure is decreased.

Similar to the electron density, the densities of Ar(4p) and Ar_2^* peak in an annulus at higher pressures and broaden towards being centre peaked as the pressure decreases. Since the lifetime of the Ar(4p) states are short (less than hundreds of nanoseconds), diffusion has little opportunity to spread excited states far from their location of production, which is maximum in and near the cathode fall. As a result, the Ar(4p) states are more tightly confined to an annulus at a given pressure than are the more mobile electrons.

Even though Ar_2^* has a shorter lifetime than Ar(4p), its density is more broadly distributed at all pressures than the visibly emitting state. This is due to the aforementioned long diffusion length of the metastable Ar(4s) which is the precursor for formation of Ar_2^*. The spatial distribution of Ar_2^* is more

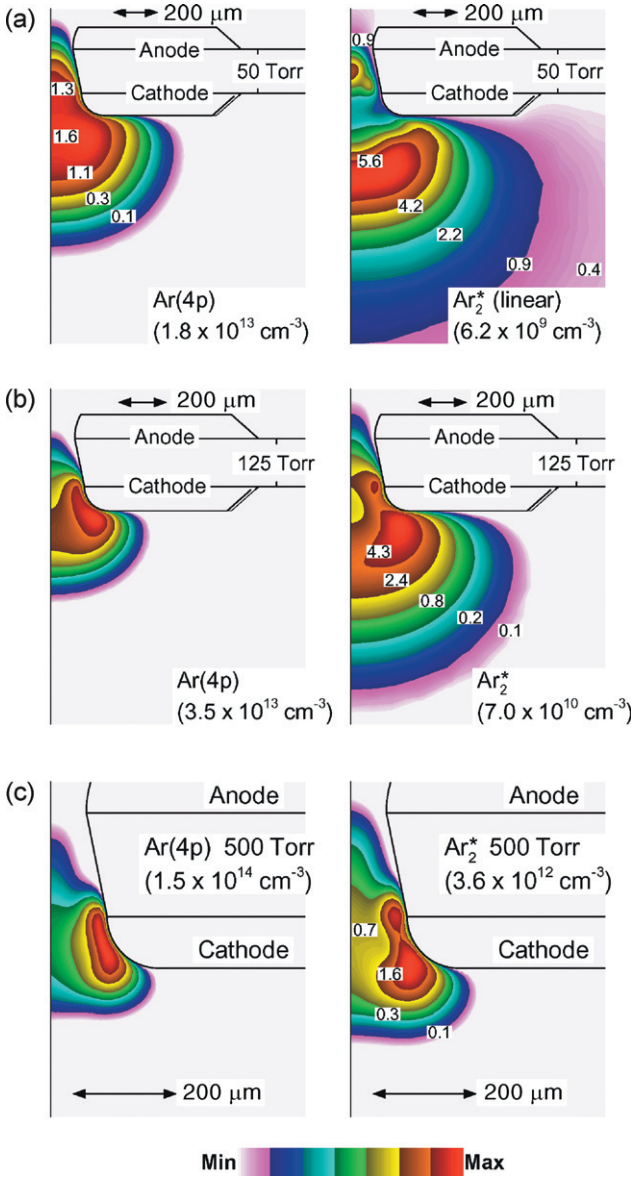

Figure 9. Densities of Ar(4p) (representing optical emission) and Ar_2^* (representing UV emission) for microdischarges operating in Ar (2 mA) for different pressures: (*a*) 50 Torr, (*b*) 125 Torr and (*c*) 500 Torr. (See figure 4 for 250 Torr.) All images are two-decade log-scale plots with maximum values indicated. The density of emitters become progressively more confined to the vicinity of the cathode as the pressure increases. The rarefaction due to gas heating, on a relative basis, is more severe at lower pressures producing a more prominent void in the rate of formation of Ar_2^*.

complex and less uniform than Ar(4p) due to rarefaction by gas heating. This non-uniform rarefaction (see, for example, figure 4) reduces the rate of formation of Ar_2^* by three-body collisions and produces a local minimum in the Ar_2^* density near the edge of the cathode where rarefaction is the greatest. As gas heating and rarefaction are (on a relative basis) more severe at lower pressure, the local minimum in the density of Ar_2^* is also more severe. For example, at 50 Torr, there are two distinct regions of high Ar_2^* density bounding the rarefied zone near the edge of the cathode. Experimental results indicate that flowing gas through the microdischarge aperture generally improves the efficiency of excimer emission [5]. These results

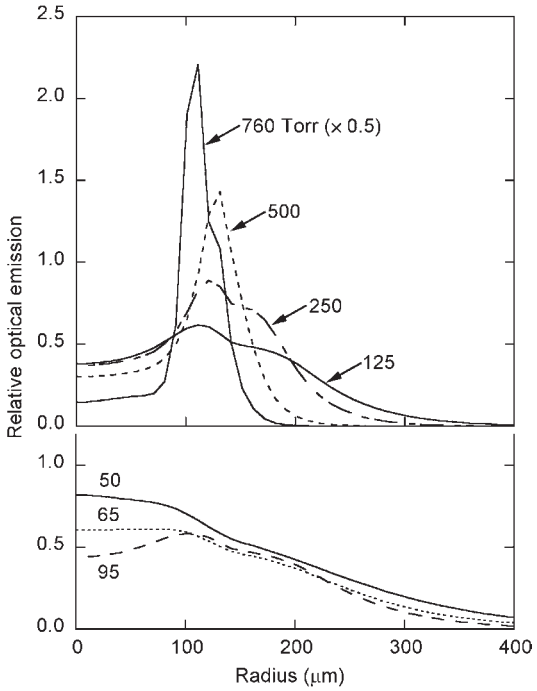

Figure 10. Relative optical visible emission as viewed from the top of the device (as approximated by the density of Ar(4p)) for microdischarges sustained in Ar (2 mA) for different pressures. The visible emission is annular at pressures above 125 Torr due to the short range of secondary electron emitted from the cathode.

may be explained by the convective heat transfer afforded by the gas flow, thereby reducing gas heating and rarefaction which detrimentally affects excimer formation.

Experimentally observed visible emission from the top and side of the MD can be approximated by performing axial and chord integrations, respectively of the density of Ar(4p) in the (r, z) plane. These integrations are shown in figure 10 for visible emission observed from the top of the device; and in figure 11 for visible emission observed from the side of the device. (Experimental results for similar conditions can be found in [3, 5].) The visible emission observed from the top of the MD has an annular peak at pressures exceeding 150–200 Torr and is centre peaked at lower pressures, in general agreement with experiments. The top view of visible emission peaks increases in peak intensity with increasing pressure in accordance with the increase of the peak Ar(4p) density.

The visible emission as observed from the side of the MD, extends ≈0.6 mm above the plane of the cathode at 50 Torr while extending barely 50 μm above the plane of the cathode at 500 Torr. These trends also agree well with experiment [3]. The side view of the visible emission has a maximum intensity at approximately 200 Torr in spite of the peak Ar(4p) density (and emission viewed from the top) increasing with pressure. These results are simply a consequence of the Ar(4p) states being progressively more confined within the central hole of the MD as the pressure increases (see figure 9) and so are only visible from the top of the device. These trends

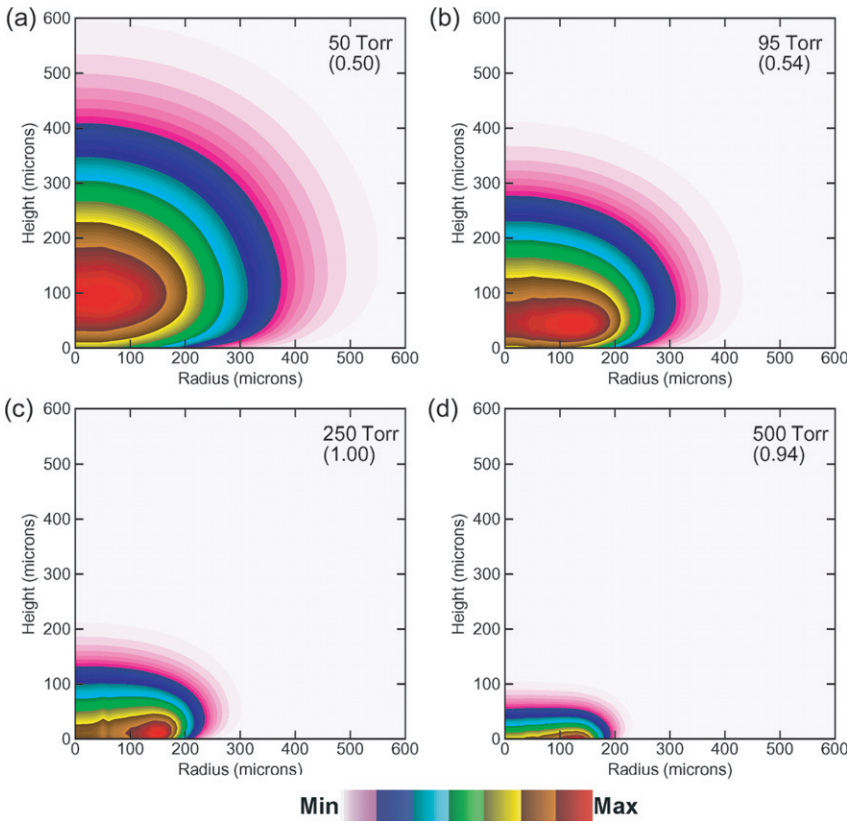

Figure 11. Relative optical visible emission as viewed from the side of the device (as approximated by the density of Ar(4p)) for microdischarges sustained in Ar (2 mA) for different pressures. (*a*) 50 Torr, (*b*) 95 Torr, (*c*) 250 Torr and (*d*) 500 Torr. The relative value of the most intense visible emission viewed from the side is noted in each figure. The visible emission extends up to 0.6 mm at low pressures. Although the absolute peak intensity emitted by the plasma increases with pressure, that intensity visible from the side is highest at about 250 Torr.

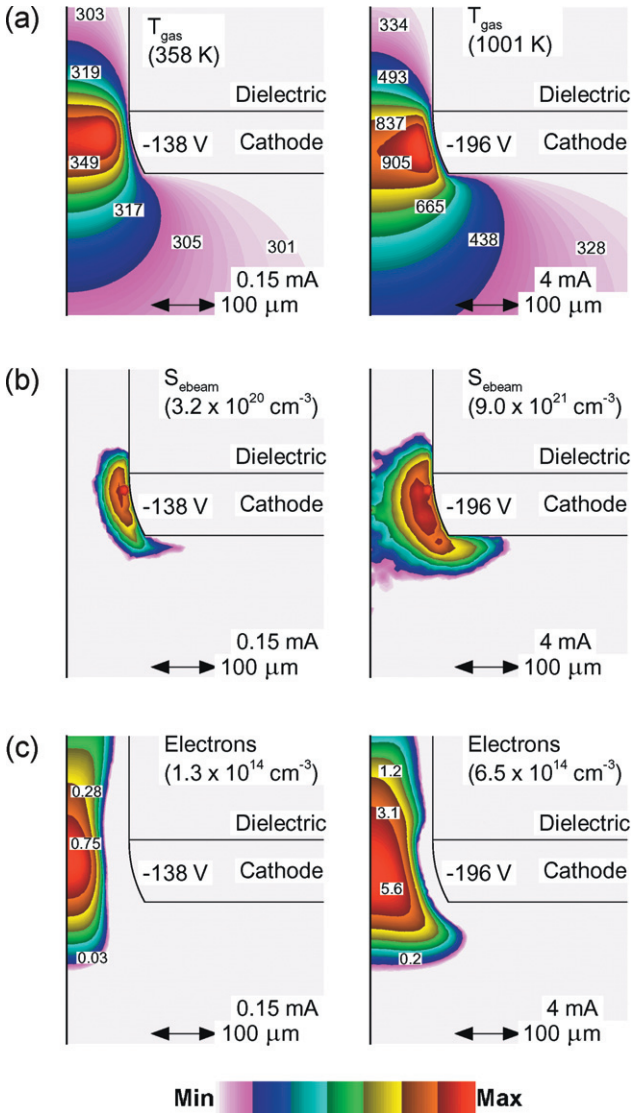

Figure 12. Plasma properties for microdischarges sustained in 250 Torr of Ar for currents of 0.15 mA and 4 mA. (*a*) Gas temperature, (*b*) electron source due to secondary electrons (three-decade, log-scale) and electron density (two-decade log-scale). The maximum value and cathode voltage is noted in each frame. Increasing cathode voltage and rarefaction due to gas heating extends the range of secondary electrons at higher currents.

are important considerations when designing MD devices for display purposes. The more intense visible emission at higher pressures has a narrow angular distribution that is dominantly perpendicular to the plane of the electrodes since it originates deeper inside the MD channel. The angular distribution of the less intense visible emission at lower pressures has a broader angular distribution, affording better side-to-side uniformity of viewing.

3.3. Scaling with current

The scaling of MD characteristics with total current is in large part dominated by gas heating. For example, the ionization sources due to beam electrons, electron density and gas temperature are shown in figure 12 for currents of

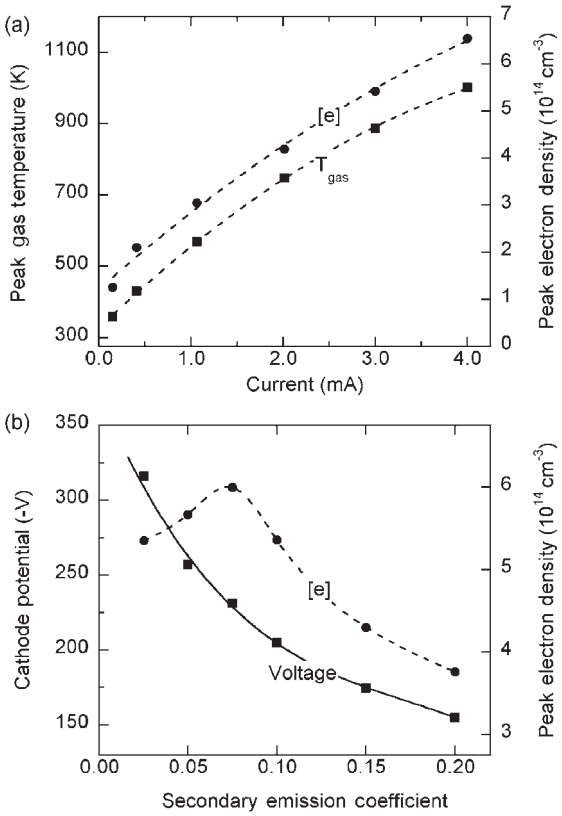

Figure 13. Plasma properties for microdischarges operating in 250 Torr Ar. (*a*) Maximum gas temperature and peak electron density as a function of current for $\gamma = 0.15$. (*b*) Cathode voltage and peak electron density as a function of secondary emission coefficient at 2 mA.

0.15 and 4 mA at a pressure of 250 Torr of Ar. The peak gas temperature and electron density as a function of current are shown in figure 13. The dielectric for these cases has a uniform, non-flaring radius of 100 μm. For these conditions, the MD resembles an abnormal glow, with the cathode voltage increasing from -138 V at 0.15 mA to -196 V at 4 mA. For this reason alone, the range of the secondary electrons accelerated in the cathode fall should increase at the higher current. The significantly greater range of the secondary electrons at 4 mA, as shown by their more extended ionization sources, is augmented by rarefaction of the gas produced by the higher gas temperature at 4 mA. The peak gas temperature increases from 360 K at 0.15 mA (60 K above ambient) to more than 1100 K at 4 mA (800 K above ambient), in general agreement with experiments by Penache *et al* [3]. Due to the low thermal mass of the system, temperature excursions can be readily controlled by modulating the current. This may provide the means to control the rate of chemical reactions by modulating the gas temperature should these MD devices be used as radical sources or chemical reactors [7].

The plasma generally extends further outside the MD hole as the current is increased, producing a similar extension in visible and UV emission, a trend also observed experimentally [1]. This extension can be in part explained by these devices having some characteristics of normal glows in which the plasma seeks more cathode area as the current increases in spite of the increase in voltage. Our results also

indicate that gas heating and rarefaction also play important roles. Larger currents result in more rarefaction over more extended volumes, enabling more efficient bulk and beam excitation.

The peak electron density also monotonically increases over this range of current, from 1.3×10^{14} cm^{-3} at 0.15 mA to 6.5×10^{14} cm^{-3} at 4 mA. This is an increase of only a factor of 5 for an increase in current exceeding 30. The additional current density is produced, in part, by the increase in cathode voltage, but is principally produced by the larger E/N afforded by rarefaction. The end result is a distribution of electron density which is fairly well confined to the axis at 0.15 mA while being more broadly distributed at 4 mA, again enabled by the rarefaction produced by gas heating.

3.4. Scaling with secondary electron emission coefficient

Given that a significant fraction of the total ionization is produced by secondary electrons, one might expect the MD characteristics to be a sensitive function of the secondary electron emission coefficient by ion impact, γ. This expectation is born out by the results in figure 13 where the peak electron density and cathode voltage are shown as a function of γ for a constant current (2 mA) and pressure (250 Torr). As γ decreases at constant current, the response of the system is to increase the cathode voltage in order to increase the total rate of ionization for the smaller flux of beam electrons. The cathode voltage increases from -155 V at $\gamma = 0.2$ to -315 V at $\gamma = 0.025$. Since the current is held constant, the total power dissipation also increases by nearly a factor of 2 as γ decreases. This increased power produces additional gas heating and rarefaction. The end result is that the peak bulk electron density also increases with moderate decreases γ. Similar sensitivities to the secondary emission coefficient were observed by Kothnur *et al* [14].

As γ decreases below 0.05, the peak electron density also begins to decrease. As the cathode voltage increases, a larger proportion of beam electrons with energies greater than the energy at which the ionization cross section is a maximum (about 100 eV) also increases. The range of the beam electrons therefore also increases. Although the total rate of ionization by beam electrons may increase, the ionization is distributed over a larger volume resulting in the peak value diminishing.

3.5. Multistage MDs

The use of MDs as for example, laser devices requires a long gain length to achieve threshold. One strategy to produce this gain length is to alternately stack cathode and anode structures in a single bore. One such design with multiple cathode–anode segments obtained positive gain in Xe [15]. The dynamics of multistage MD devices of the dimensions and operating conditions of interest (100–200 μm diameter, a few milliamperes, many hundreds of Torr) can be dominated by gas rarefaction and transport. It should not be unexpected that subtle differences in the design of multistage devices may be magnified by these thermodynamic considerations.

To illustrate these points, plasma properties (ionization by beam electrons, electron density, gas temperature and gas flow field) for two MD devices, each having two sets of cathode–anode electrodes, are shown in figures 14 and 15. The first MD has a straight dielectric separating the top and bottom sets of electrodes. The second MD has an indentation in the dielectric. The pressure is 250 Torr Ar with total current of 2 mA. A single resistor ballasts both cathodes.

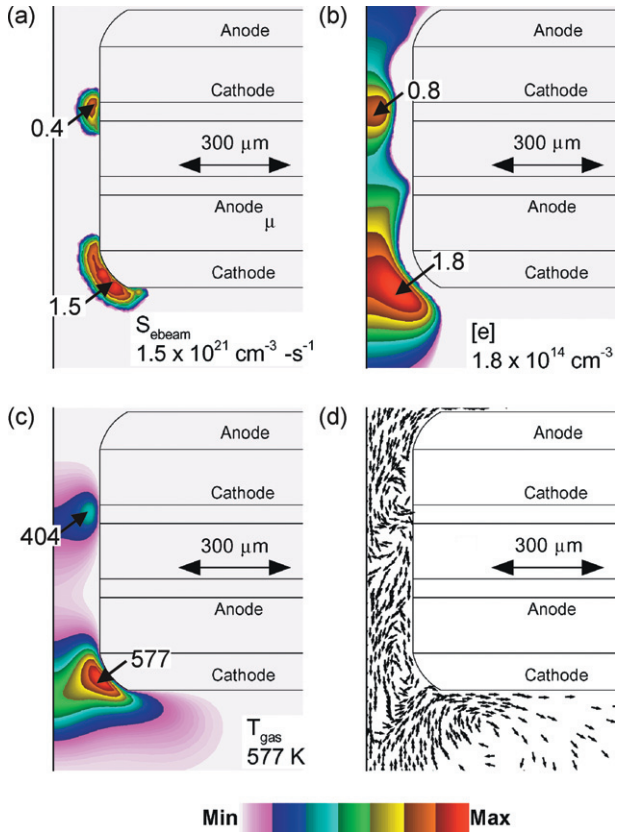

Figure 14. Plasma properties for a multistage microdischarge operating in 250 Torr Ar with straight dielectric walls. (*a*) Electron ionization source by secondary electrons (three-decade log plot), (*b*) electron density (two-decade log plot), (*c*) gas temperature and (*d*) vector direction of gas flow field. The maximum values in each frame are noted in the figures. The maximum downward gas speed is 20.1 m s^{-1}.

The peak electron densities are similar in both cases, 1.6–1.8 $\times 10^{14}$ cm^{-3} and occur near the lower cathode which are structurally the same. The secondary peak in electron density near the upper cathode significantly differ, an effect that is partly attributed to differences in gas heating. The MD with a straight dielectric has only moderate heating (100 K above ambient) adjacent to the upper electrode due to there being better heat transfer to the walls. This produces less rarefaction, a lower E/N and smaller ionization sources. More current is therefore proportionally channelled through the lower cathode, which produces more gas heating (277 K above ambient) and rarefaction. The end result is a peak in electron density near the upper cathode of only 0.8×10^{14} cm^{-3} compared to 1.8×10^{14} cm^{-3} adjacent to the lower cathode. A cathode potential of -208 V is required to deliver 2 mA. The gas speed peaks at 20 m s^{-1} downwards with moderate recirculation near the upper cathode.

The MD with the reentrant dielectric has plasma properties that are more similar near the two cathodes. With the reentrant gas plenum, the heat transfer characteristics around the upper and lower cathodes are similar, producing nearly the same peak

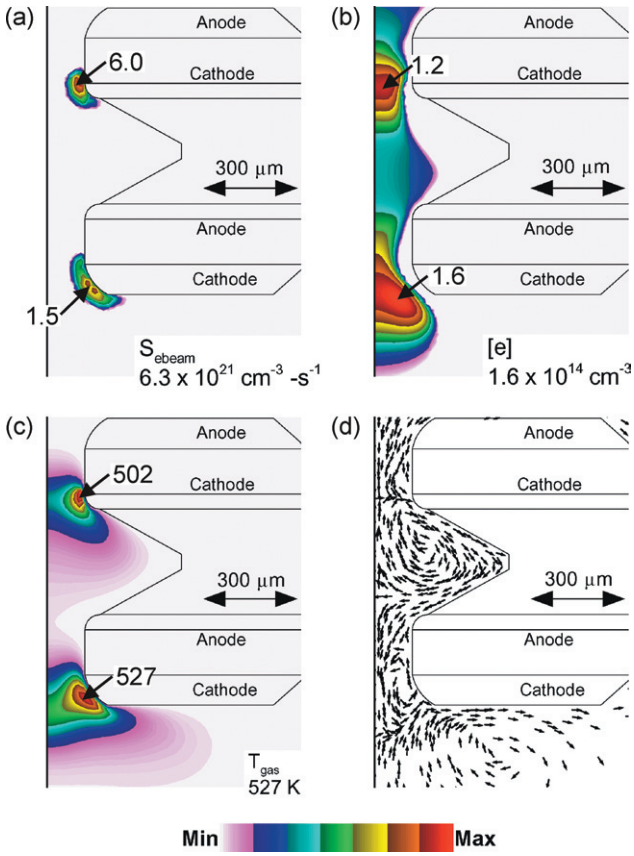

Figure 15. Plasma properties for a multistage microdischarge operating in 250 Torr Ar with reentrant dielectric walls. (*a*) Electron ionization source by secondary electrons (three-decade log plot), (*b*) electron density (two-decade log plot), (*c*) gas temperature and (*d*) vector direction of gas flow field. The maximum values in each frame are noted in the figures. The maximum downward gas speed is 18.1 m s^{-1}.

gas temperatures, rarefaction and E/N. Current is therefore more equitably shared between the two cathodes, producing an electron density near the upper cathode of 1.2×10^{14} cm^{-3} compared to 1.6×10^{14} cm^{-3} near the lower cathode. As a result, there is a more equitable sharing of current and a smaller cathode potential of -199 V is required to deliver 2 mA. There is considerable recirculation within the plenum, which reduces the downward directed gas flow to a peak speed of 18 m s^{-1}.

4. Concluding remarks

The dynamics of cylindrical, metal–dielectric–metal sandwich MDs have been computationally investigated. These devices share many of the characteristics of their macroscopic, negative glow counterparts, particularly with respect to being sustained by secondary electron emission from the cathode. As a consequence, these MDs are particularly sensitive to variations in the secondary electron emission coefficient by ions and, in some case, by photons. This dependence will likely translate into the devices being sensitive to small changes in γ resulting from aging. The MDs have the added feature of being able to operate as glow discharges on a cw basis with large current densities and power deposition. As a result, gas heating and flow dynamics are important considerations in optimizing the electrical and kinetic properties of the devices. For example, the formation of excimer species is particular sensitive to gas heating and rarefaction due to their dependence on three-body formation processes. These dynamics also affect the visible and UV emission characteristics of the devices. For example, the viewing angle of visible and excimer emission differ and have different functional dependencies on pressure due to the location within the MD that their respective excited states are formed. Operation at higher pressures, produces higher peak densities of both species located deeper within the MD device which, as a result, have smaller view angles.

Acknowledgments

This work was supported by the National Science Foundation (CTS 03-15353) and the Air Force Research Laboratory.

References

[1] Schoenbach K H, E-Habachi A, Shi W and Ciocca M 1997 *Plasma Sources Sci. Technol.* **6** 468
[2] Park S J, Chen J, Wagner C J, Ostron N P, Liu C and Eden J G 2002 *IEEE Select. Top. Quant. Electron.* **8** 387
[3] Penache C, Miclea M, Brauning-Demian A, Hohn O, Schossler S, Jahnke T, Niemax K and Schmidt-Bocking H 2002 *Plasma Sources Sci. Technol.* **11** 476
[4] Adler F, Davliatchine E and Kindel E 2002 *J. Phys. D: Appl. Phys.* **35** 2291
[5] Moselhy M, Petzenhauser I, Frank K and Schoenbach K H 2003 *J. Phys. D: Appl. Phys.* **36** 2922
[6] Sankaran R M and Giapis K P 2003 *J. Phys. D: Appl. Phys.* **36** 2914
[7] Hsu D D and Graves D B 2003 *J. Phys. D: Appl. Phys.* **36** 2898
[8] Sankaran R M and Giapis K P 2002 *J. Appl. Phys.* **92** 2406
[9] Boeuf J P 2003 *J. Phys. D: Appl. Phys.* **36** R53
[10] Lay B, Moss R S, Rauf S and Kushner M J 2003 *Plasma Sources Sci. Technol.* **12** 8
[11] Kushner M J 2004 *J. Appl. Phys.* **95** 846
[12] Bhoj A and Kushner M J 2004 *J. Phys. D: Appl. Phys.* **37** 2510
[13] Leiby C C and Oskam H J 1967 *Phys. Fluids* **10** 1993
[14] Kothnur P S, Yuan S Y and Raja L L 2003 *Appl. Phys. Lett.* **82** 529
[15] von Allmen P, Sadler D J, Jensen C, Ostrom N P, McCain S T, Vojak B A and Eden J G 2003 *Appl. Phys. Lett.* **82** 4447